

RESEARCH ARTICLE

Analytical description of the distributions of primary and secondary cosmogenic particles

Shvetaank Tripathi^{1,2} | Prashant Shukla^{1,2}

¹Nuclear Physics Division, Bhabha Atomic Research Centre, Mumbai, Maharashtra, India

²Homi Bhabha National Institute, Mumbai, Maharashtra, India

Correspondence

Corresponding authors: Prashant Shukla; Shvetaank Tripathi.

Email: pshukla@barc.gov.in;
shvetaank05@gmail.com

Abstract

In this work, we present an analytical description of the energy distributions of primary and secondary cosmogenic particles on Earth in terms of parameters having clear physical meaning. A modified power law is assumed for energy distributions, incorporating terms such as energy loss/decay, which are effective at low energies, and a source term, which is dominant at high energies. The parametrizations of the momentum distribution of primary protons and helium have been obtained including energy loss term. For muons, both the energy loss and decay terms have been included. It is shown analytically that zenith angle distributions is given by $\cos^{n-1} \theta$ in terms of energy index n and the presence of decay term does not affect it. The analytical function describes the muon momentum distribution data at different altitudes and zenith angles. The same form is also applied to describe the atmospheric muon and electron-type neutrino distributions simulated at various sites. The presented analytical functions provide an excellent description of all kinds of cosmogenic particles.

KEY WORDS

cosmic rays; muon; pion; neutrino

1 | INTRODUCTION

Soon after their discovery^{1,2,3,4,5,6,7}, the study of cosmic rays and their interactions with Earth's atmosphere became an active area of research⁸. Numerous experiments have been conducted worldwide to investigate their origin, acceleration mechanisms, propagation, and ionization effects^{9,10,11,12,13,14,15,16,17,18,19,20,21,22,23}. It is now understood that cosmic rays originate from astrophysical events such as supernovae, active galactic nuclei, pulsars, and gamma-ray bursts, gaining energy via acceleration in intergalactic magnetic fields. They strike Earth's atmosphere at a rate of approximately 1000 particles per square meter per second. Most of the detected cosmic rays originate within our galaxy, as extra-galactic particles are largely deflected by the Galactic magnetic field. Additionally, the Sun's magnetic field prevents low-energy particles with $E < 1$ GeV from reaching Earth. Cosmic rays are ionized atomic nuclei, composed primarily of protons (~90%) and alpha particles (~9%), with the remaining fraction consisting of heavier nuclei.

Upon entering Earth's atmosphere, cosmic ray particles undergo high-energy collisions with air nuclei. These interactions generate showers of secondary particles, predominantly pions and kaons, along with hyperons, nucleon-antinucleon pairs, and small fractions containing charm quarks²⁴. Subsequent decay of these secondary particles leads to the formation of Extensive Air Showers (EAS), comprising hadronic, mesonic, and electromagnetic components. The shower contains both charged and neutral particles, many of these having finite lifetime but still reach sea level due to relativistic effects. As the charged particles propagate, they continuously lose energy via processes like ionization and interactions with nuclei. The ionization losses decrease as the energy of the particle increases and become almost constant. At very high energies the radiative losses become dominant. The electromagnetic cascades which result from pair production and bremsstrahlung, were formally described by Bethe and Heitler²⁵.

Abbreviations: EAS, Extensive Air Shower.

The flux distribution for primary cosmogenic particles is observed to follow the power law, i.e.

$$\frac{dN}{dE} \propto E^{-n}, \quad (1)$$

where n denotes the spectral index which carries the value ≈ 2.7 in wide energy range. The power law is also applied to the secondary particles produced in shower. Use of such power-law spectrum may have helped in calculations regarding pion spectrum which led to the formulation of the linear development of a cascade of particles in the atmosphere. This work is extensively explained in²⁶.

The power law grossly explains the momentum distribution of particles at high energies, but at lower energies the effect of interactions must be taken into account. Numerical calculations are normally performed to account accurately for decay and energy loss processes along with the knowledge of primary cosmic spectrum and the energy dependencies of their interaction cross-sections. In recent years, several semi-analytical models^{26,27,28} have been proposed aiming to describe cosmogenic particles and their interactions in Earth's atmosphere. Theoretical calculations^{29,30,31} and transport models^{32,33} provided detailed investigations regarding spectra for secondary cosmogenic particles. In addition, Monte Carlo codes such as CORSIKA³⁴ employ different models to calculate the interactions of cosmic particles in the Earth's atmosphere³⁵. Recent advances in muon spectrum calculations have significantly enhanced our understanding of cosmic ray interactions for underground^{36,37,38} and atmospheric physics^{39,40,41}. The IceCube Collaboration recently conducted an extensive analysis of seasonal variations in the atmospheric muon neutrino spectrum, using 11.3 years of data, reporting energy-dependent variations in agreement with theoretical predictions^{42,43}.

The aim of this work is to derive simple analytical formulae to describe the momentum distributions of primary and secondary particles. These functions incorporate realistic features of the distributions through parameters with clear physical significance. The resulting expressions can be both practical and useful in various applications, such as serving as input for detector simulations in cosmic ray experiments and searches for rare physical phenomena. Moreover, analytical expressions can be used to extrapolate measured data in unknown regions and obtain integrated flux. This work can be considered an extension of the study presented in⁴⁴.

For primary particles, we introduce an energy loss term that is significant at lower energies but becomes negligible at higher energies. For secondary particles such as muons, we incorporate an exponentially decaying function to account for their reduced abundance at lower energies. Additionally, we include dependencies on key variables such as atmospheric depth and zenith angle. Using these formulations, we determine the values of the parameters with experimental data collected worldwide for protons and helium^{9,10,11,12,13,14,15,16,17,18}, as well as for muons^{45,46,47,48,49,50,51,52}. Furthermore, we analyze variations in muon flux with atmospheric depth and zenith angle using our modified formulation, fitting it to experimental data from Bellotti⁵³ et al. and the L3 collaboration⁵⁴. We extend this formula to neutrinos by incorporating a source term instead of a decay function, reflecting their stability and minimal interactions.

The structure of this paper is as follows: Section 2 discusses the description of the flux distribution for primary particles and comparison with previous results. Section 3 presents the description of energy and zenith angle distributions for muons. Section 4 presents studies of variations in muon flux with atmospheric depth and zenith angle. In Section 5, we extend the formulation to atmospheric neutrinos. Finally, Section 6 provides a summary of our findings.

2 | FLUX DISTRIBUTION OF PRIMARY COSMIC PARTICLES

The flux for primary and secondary cosmogenic particles as a function of energy has been described in⁴⁴ as:

$$I(E) = I_0 N (E_0 d + E)^{-n} \left(1 + \frac{E}{\epsilon} \right)^{-1}, \quad (2)$$

where $E_0 d$ could be the energy loss by particles, N is the normalisation constant obtained numerically, n represents the spectral index and I_0 is the integrated flux, given by $I_0 = \int_{E_c}^{\infty} I(E) dE$, with E_c being the lower cut-off energy of the data. The parameter ϵ was added to modify the power in the high energy part which should account for the finite lifetimes of pions and kaons.

The parameters of Eq. 2, as obtained by fitting the measured distributions for primary protons and helium, have already been given in⁴⁴. This distribution does not give good distribution of data at lower energies where the flux is suppressed. Hence, a new

modified distribution function for primary particles is proposed:

$$I(E) = I_0 N \left(\frac{E_1}{E} + E \right)^{-n}. \quad (3)$$

Primary particles, such as protons and helium, might experience energy loss while propagating through the cosmos and the upper layers of the atmosphere. The introduction of the term E_1/E for primary particles is motivated by the energy loss experienced by massive charged particles as they traverse the atmosphere. At lower energies, the rate of energy loss through ionization and other electromagnetic processes increases approximately as $1/E$ as we move down in energy, leading to a suppression of the spectrum. The inclusion of the E_1/E term effectively accounts for this low-energy attenuation. Here the unit of E_1 is GeV^2 .

Figure 1 shows Proton and Helium flux^{9,10,11,12,13,14,15,16,17,18} as a function of momentum, fitted with Eq. 3. The parameters obtained by fitting proton and helium data are given in Table 1. The value of spectral index, n comes out to be near 2.7 for both the primary particles. The higher values of χ^2/NDF can also be attributed to the fact that we have combined data from multiple experiments, as no single experiment covers the entire energy range. This function provides a good description of energy distribution for primary particles with energy as low as 1 GeV. The exact production processes of primary particles and their interactions in the intergalactic media are difficult to be determined, especially the spectral shape at low energy.

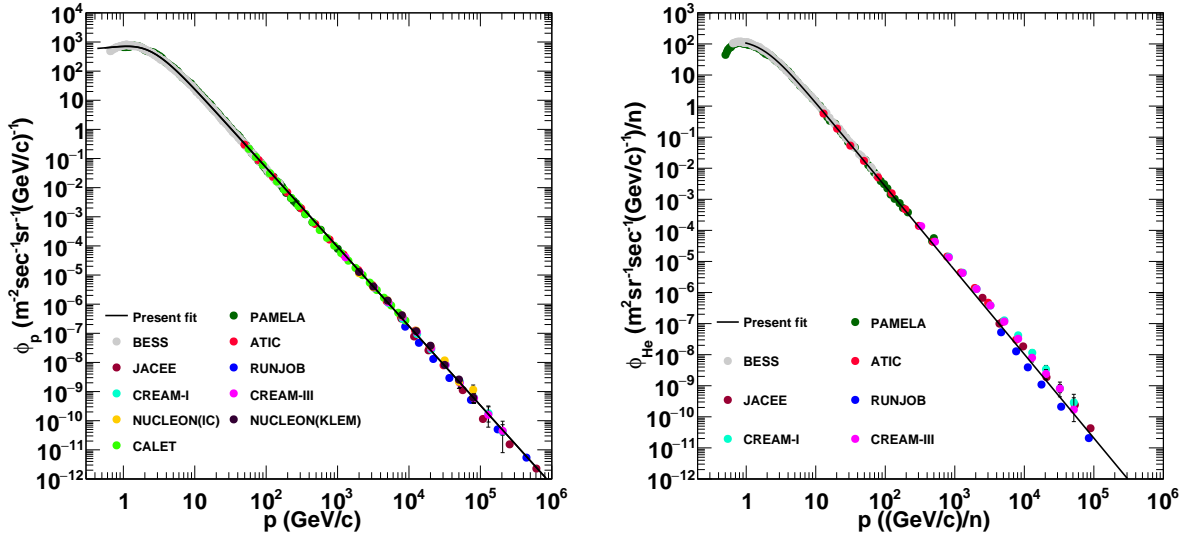


FIGURE 1 Proton and Helium flux^{9,10,11,12,13,14,15,16,17,18} as a function of momentum, fitted with Eq. 3.

TABLE 1 Parameters obtained by fitting proton and helium data with Eq. 3.

	I_0 ($\text{m}^{-2} \text{ s}^{-1} \text{ sr}^{-1}$)	E_1 (GeV^2)	n	χ^2/NDF	Data Reference
Protons	2606.68 ± 36.87	2.16 ± 0.02	2.72 ± 0.04	10.02	9,10,11,12,13,14,15,16,17,18
Helium	289.24 ± 4.96	0.80 ± 0.02	2.70 ± 0.04	5.81	9,10,11,12,13,14,15,16,17,18

3 | FLUX DISTRIBUTION OF ATMOSPHERIC MUONS

In this section, we study energy and zenith angle distribution of muons. The distribution of secondary cosmogenic particles such as muons has been described by Eq. 2 which is given in⁴⁴. The parameters of the distribution, corresponding to data collected

from various experiments are also given in⁴⁴. The comparison of measured data for muons at various locations along with parametrized function (Eq. 2) with various combinations of low-energy and high-energy models (GEISHA & QGSJET, UrQMD & QGSJET, UrQMD & QGSJET-II, GEISHA & SIBYLL, UrQMD & SIBYLL and FLUKA & SIBYLL) was done in Ref.³⁵(see fig. 2, 3, 4). This work attempted to use a modified power law which works at lower energies. However, it does not account for the decaying nature of particles like muons. While high-energy muons can travel large distances, lower-energy muons tend to decay into electrons or positrons, producing the neutrinos and anti-neutrinos.

3.1 | Energy Distribution

We propose a modified energy distribution function to describe muon momentum distribution which includes effect of decay of muons:

$$I(E) = I_0 N \left(\frac{E_0 d}{\cos \theta} + E \right)^{-n} \exp \left(-\frac{k}{E \cos \theta} \right), \quad (4)$$

where variables d and θ represent the atmospheric depth and zenith angle, respectively, ensuring that the function captures variations in flux distribution with respect to these variables. The exponential term accounts for decay of muons which can be understood as follows. A particle travelling with velocity β will cover a distance $\beta \gamma \tau c$ during its lifetime τ . This leads to the decay rate per mean free path, λ_d , expressed as

$$\frac{1}{\lambda_d} = \frac{1}{\beta \gamma \tau c} = \frac{m}{\tau p c}, \quad (5)$$

where m is the mass of the particle and p is its momentum.

Using this, we compute the survival probability of the particle after traversing a thickness X along an inclined trajectory with zenith angle θ :

$$S = \exp \left(- \int \frac{m}{\tau p c \cos \theta} dX \right). \quad (6)$$

For muons, the survival probability at a given energy, E in a fixed small distance, dX can be written as:

$$S \approx \exp \left(-\frac{k}{E \cos \theta} \right), \quad (7)$$

where k is a parameter encapsulating all constant factors (m, τ) leaving only E and $\cos \theta$. The parameter k depends on the mass and lifetime of the particle and governs the flux loss at lower energies. The exponential term in the proposed analytical function reflects the same physical mechanism predicted by cascade theory, the progressive depletion of low energy muons due to decay before reaching the observation level, while at higher energies, the contribution becomes negligible, leaving the power-law behaviour dominant. For vertical muons, the exponential term becomes ~ 1 above energy 18 - 20 GeV. It also depends upon the zenith angles, eg. at 60° zenith angle range, the energy at which the exponential terms become ~ 1 increases to ~ 35 - 40 GeV.

Figure 2 shows the muon flux as a function of momentum at various locations^{45,46,47,48,49,50,51,52}, fitted with Eq. 4. We have also included the parametrization done by T.K. Gaisser (see Ch.6 of²⁶), which gives a good fitting at higher momentum but fails at lower momentum. In contrast, the present function provides a better fit in the whole range of momentum. The values of parameters obtained after fitting muon distributions with Eq. 4, keeping $E_0 d$ and k as free, are given in Table 2. Comparison between present fit (Eq. 4) and Gaisser Parametrization is also shown in terms of χ^2/NDF values for both models. The spectral index n is slightly larger than that observed for primary particles. The value of k lies between 0.10 to 0.35 GeV. It can have a correlation with $E_0 d$. The value of $E_0 d$ in general decreases with increasing altitude and increases with zenith angle. This analysis helps to obtain the integrated flux, given by I_0 , from measured data which requires extrapolation. The function given by Eq. 4 works well in case of muons in the low energy range, as low as 200 MeV. Data for muons below this energy are not available which can be due to measurement difficulties.

3.2 | Zenith Angle Distribution

The modified energy distribution function for muons, as defined in the previous subsection, also depends on the zenith angle, θ . Using Eq. 4, we can obtain the energy-integrated flux, $\phi(\theta)$, at a given zenith angle θ as:

$$\phi(\theta) = I_0 N \int_0^\infty \left(\frac{E_0 d}{\cos \theta} + E \right)^{-n} \exp \left(-\frac{k}{E \cos \theta} \right) dE. \quad (8)$$

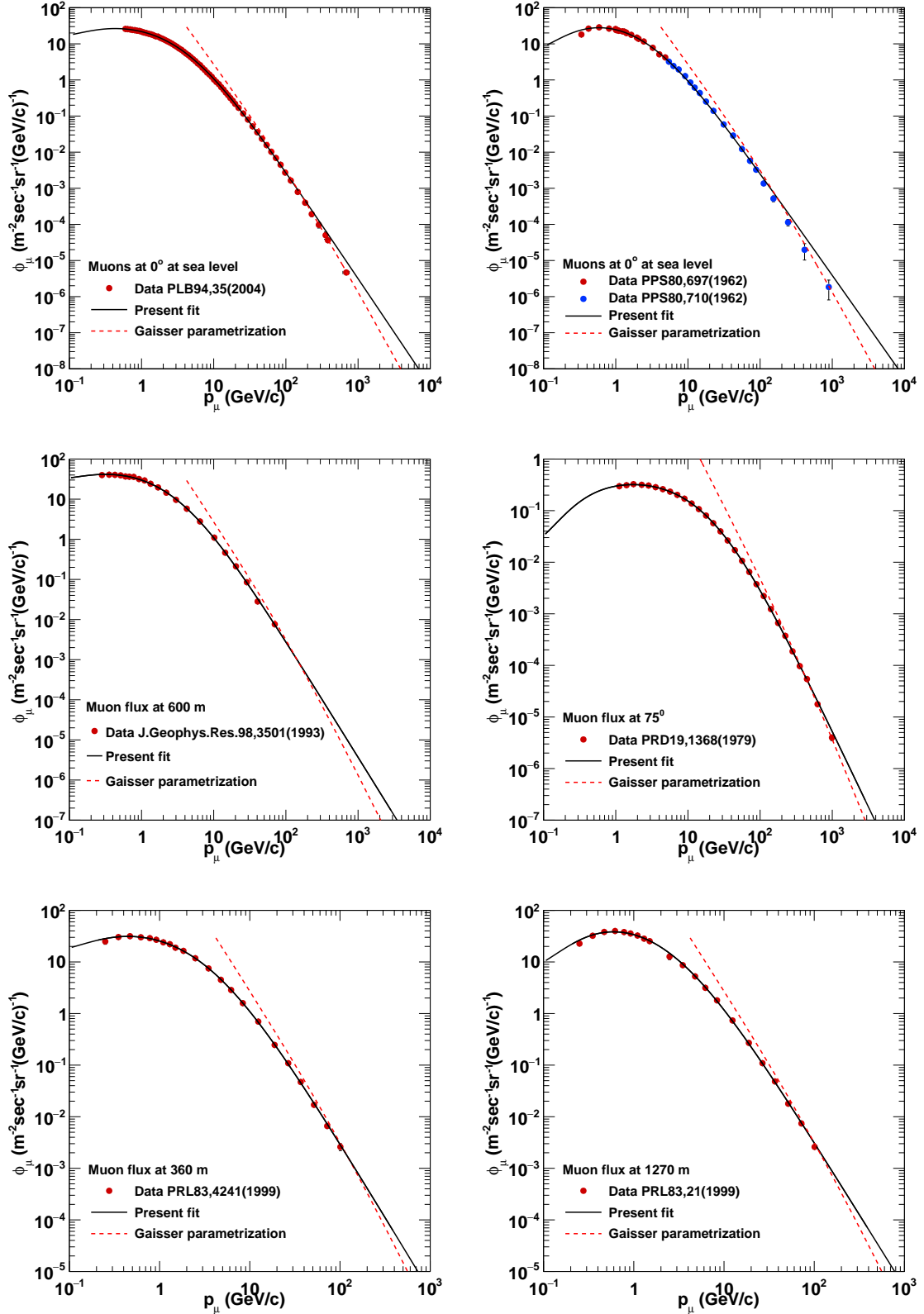


FIGURE 2 Muon flux as a function of momentum at various locations^{45,46,47,48,49,50,51,52}, fitted with Eq. 4.

TABLE 2 Parameters obtained after fitting muon distributions with Eq. 4, keeping $E_0.d$ and k as free. Comparison between present fit (Eq. 4) and Gaisser Parametrization²⁶ is shown in terms of χ^2/NDF values for both models.

	I_0 ($\text{m}^{-2} \text{s}^{-1} \text{sr}^{-1}$)	$E_0.d$ (GeV)	n	k (GeV)	χ^2/NDF Present Fit	Gaisser Param.	Data Reference
μ at 0°	81.35	3.82	2.98	0.14	0.90	8.90	Tsukuba, Japan
at sea level	± 4.28	± 0.07	± 0.01	± 0.02			(36.2° N, 140.1° W) ⁴⁵
μ at 0°	80.23	2.58	2.84	0.32	12.56	63.34	Durham, UK
at sea level	± 3.76	± 0.05	± 0.01	± 0.01			(54.76° N, 1.57° W) ^{47,48}
μ at 0°	103.69	3.06	2.90	0.10	1.91	72.28	Prince Albert, Canada
at 600 m	± 13.12	± 0.13	± 0.04	± 0.02			(53.2° N, 105.75° W) ⁴⁹
μ at 75°	4.83	5.39	2.95	0.10	1.01	37.02	Hamburg, Germany
at sea level	± 0.44	± 0.09	± 0.02	± 0.01			(53.56° N, 10° E) ⁵⁰
μ at 0°	90.10	3.24	2.90	0.16	0.728	71.54	Lynn Lake, Canada
at 360 m	± 2.48	± 0.12	± 0.03	± 0.02			(56.5° N, 101.0° W) ⁵¹
μ at 0°	106.69	2.36	2.82	0.35	1.981	8.89	Fort Sumner, New Mexico
at 1270 m	± 2.64	± 0.09	± 0.02	± 0.02			(34.3° N, 104.1° W) ⁵¹

Substituting, $E \cos \theta = x$ and $dE = dx/\cos \theta$, we have

$$\phi(\theta) = \cos^{n-1} \theta \times I_0 N \int_0^\infty (E_0 d + x)^{-n} \exp\left(-\frac{k}{x}\right) dx = \cos^{n-1} \theta \times \phi(0), \quad (9)$$

where $\phi(0)$ is the vertical intensity of muons. This gives an analytical expression for the ratio of energy-integrated flux for muons coming at zenith angle, θ with that for vertical muons as

$$\frac{\phi(\theta)}{\phi(0)} = \cos^{n-1} \theta. \quad (10)$$

This shows that the decay term in the muon flux distribution does not affect the zenith angle distribution which effectively gets canceled out in the ratio. With energy index $n \sim 3$, we get the $\cos^2 \theta$ distribution which is empirically shown to hold good with various measurements over time.

4 | VARIATION IN MUON FLUXES WITH RESPECT TO ATMOSPHERIC DEPTH AND ZENITH ANGLE

The modified function for the distribution of muons given by Eq. 4 includes dependencies on atmospheric depth (d) and zenith angle (θ). We use this function to describe negative muon flux as a function of momentum measured at different atmospheric depths⁵³ and obtain the parameters E_0 and k . The value of θ is taken to be 0° while studying the variation with atmospheric depth. The L3 experiment⁵⁴ measured distributions of both the positive and negative muons at different zenith angles at an altitude 450 m above sea level which corresponds to a value of $d = 967 \text{ g/cm}^2$. We use this data to obtain the parameters of Eq. 4 as a function of zenith angle.

4.1 | Variation with respect to atmospheric depth :

In this section, we analyze the muon flux distributions at various atmospheric depths. First, the value of E_0 is kept fixed to be 0.002 GeV/g-cm^2 which is close to the value of energy loss for minimum ionizing particles and k is kept free. Figure 3 shows the negative muon flux as a function of momentum measured at different atmospheric depths⁵³. In this analysis, the zenith angle, θ is fixed at 0° . The solid lines are obtained by fitting the data with Eq. 4 keeping $E_0 = 0.002 \text{ GeV/g-cm}^2$ and k free. Table 3 shows the values of parameters obtained.

The value of k , as substituted in Eq. 7, depends on the total distance travelled by a muon, along with the constants such as mass and lifetime of muon and speed of light. This gives a value of k between 0.16 to 1.6 GeV for muons travelling the distance of 1 to 10 kms. The value of k obtained by fitting lies between 0.69 GeV to 0.88 GeV with small variation and hence we fix it to a value 0.80 GeV. Figure 4 shows the negative muon flux as a function of momentum at different atmospheric depths⁵³.

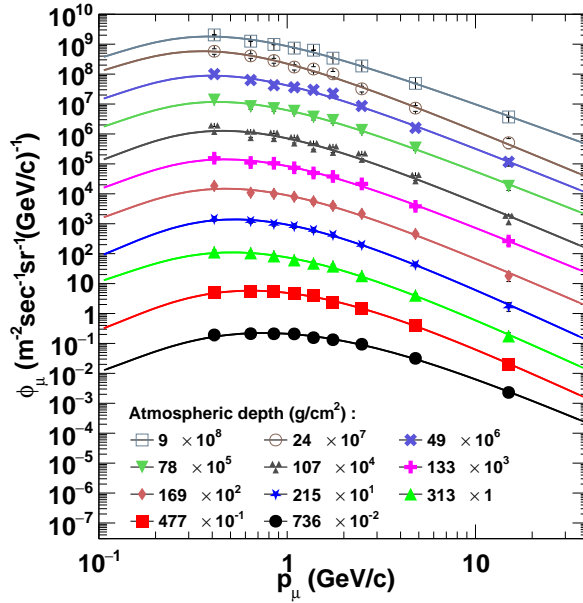


FIGURE 3 The negative muon flux as a function of momentum measured at different atmospheric depths⁵³. The solid lines are obtained by fitting the data with Eq. 4 keeping $E_0 = 0.002 \text{ GeV/g-cm}^{-2}$ and k free.

TABLE 3 The values of parameters obtained by fitting the data of negative muon momentum distribution at different atmospheric depths⁵³ with $E_0 = 0.002 \text{ GeV/g-cm}^{-2}$ and k free.

Atmospheric depth (g/cm ²)	I_0 (m ⁻² s ⁻¹ sr ⁻¹)	E_0 (GeV/g-cm ⁻²)	n	k (GeV)	χ^2/NDF
736	60.521 ± 24.585	0.002	2.70 ± 0.19	0.695 ± 0.236	0.122
477	112.119 ± 32.802	0.002	2.94 ± 0.12	0.779 ± 0.166	0.177
313	164.766 ± 44.553	0.002	2.91 ± 0.15	0.691 ± 0.164	0.248
215	196.095 ± 53.801	0.002	2.93 ± 0.16	0.872 ± 0.182	0.258
169	198.829 ± 57.901	0.002	2.75 ± 0.16	0.788 ± 0.204	0.890
133	191.673 ± 53.564	0.002	2.62 ± 0.16	0.808 ± 0.197	0.485
107	161.134 ± 45.232	0.002	2.68 ± 0.16	0.856 ± 0.206	0.813
78	148.316 ± 40.189	0.002	2.51 ± 0.15	0.812 ± 0.200	0.527
49	101.676 ± 26.034	0.002	2.55 ± 0.15	0.847 ± 0.191	1.263
24	56.986 ± 18.329	0.002	2.64 ± 0.21	0.866 ± 0.253	0.502
9	22.121 ± 0.847	0.002	2.30 ± 0.02	0.879 ± 0.032	0.168

The solid lines are obtained by fitting the data with Eq. 4 keeping $E_0 = 0.002 \text{ GeV/g-cm}^{-2}$ and $k = 0.80 \text{ GeV}$. Table 4 shows the values of parameters obtained. The parametrization allows calculation of the integrated flux, I_0 . In case of depth variation, it is the integrated vertical flux for the negative muon and should be around half of the total muon integrated flux. At a depth of 736 g/cm² (altitude $\sim 3 \text{ km}$), the flux is $59.89 \text{ m}^{-2}\text{s}^{-1}\text{sr}^{-1}$, higher than that at sea level. The integrated flux I_0 first increases with increasing depth and then after reaching a certain point, it begins to decrease. Additionally, the value of n is 2.76 near the Sea level, but it increases slightly with altitude before decreasing again, indicating that the muon spectrum hardens at higher altitudes.

4.2 | Variation with respect to zenith angle :

The set of fixed values for E_0 and k that have been used in last subsection gives good description of the muon flux distributions as a function of depth but do not reproduce the data as a function of zenith angle variation. Thus, we fixed the value of k first to

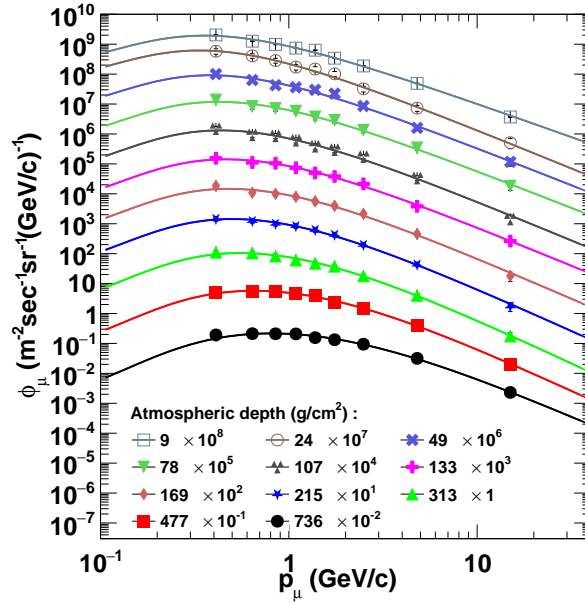


FIGURE 4 The negative muon flux as a function of momentum measured at different atmospheric depths⁵³. The solid lines are obtained by fitting the data with Eq. 4 keeping $E_0 = 0.002 \text{ GeV/g-cm}^{-2}$ and $k = 0.80 \text{ GeV}$.

TABLE 4 The values of parameters obtained by fitting the data of negative muon momentum distribution at different atmospheric depths⁵³ with $E_0 = 0.002 \text{ GeV/g-cm}^{-2}$ and $k = 0.80 \text{ GeV}$.

Atmospheric depth (g/cm ²)	I_0 (m ⁻² s ⁻¹ sr ⁻¹)	E_0 (GeV/g-cm ⁻²)	n	k (GeV)	χ^2/NDF
736	59.887 ± 11.437	0.002	2.76 ± 0.12	0.80	0.131
477	111.848 ± 13.434	0.002	2.96 ± 0.09	0.80	0.557
313	161.489 ± 15.489	0.002	2.99 ± 0.09	0.80	0.273
215	198.513 ± 15.905	0.002	2.88 ± 0.08	0.80	0.244
169	198.312 ± 16.020	0.002	2.75 ± 0.08	0.80	0.763
133	191.993 ± 15.076	0.002	2.62 ± 0.08	0.80	0.416
107	163.274 ± 12.346	0.002	2.64 ± 0.07	0.80	0.707
78	148.761 ± 11.190	0.002	2.50 ± 0.07	0.80	0.451
49	102.989 ± 6.425	0.002	2.51 ± 0.06	0.80	1.091
24	58.465 ± 4.329	0.002	2.59 ± 0.08	0.80	0.440
9	22.762 ± 2.295	0.002	2.26 ± 0.01	0.80	0.153

TABLE 5 The values of parameters obtained by fitting the total muon momentum distribution at different zenith angles⁵⁴ with $E_0 = 0.005 \text{ GeV/g-cm}^{-2}$ and $k = 0.80 \text{ GeV}$. Atmospheric depth, d is fixed at 967.0 g/cm².

Zenith Angle (degrees)	I_0 (m ⁻² s ⁻¹ sr ⁻¹)	E_0 (GeV/g-cm ⁻²)	n	k (GeV)	χ^2/NDF
9.07	69.770 ± 5.768	0.005	3.28 ± 0.00	0.80	1.537
16.96	67.445 ± 7.412	0.005	3.28 ± 0.01	0.80	0.993
23.22	64.601 ± 6.688	0.005	3.28 ± 0.01	0.80	1.194
30.40	59.513 ± 6.444	0.005	3.29 ± 0.01	0.80	1.718
38.05	50.436 ± 6.033	0.005	3.29 ± 0.01	0.80	1.864
44.56	39.285 ± 4.352	0.005	3.26 ± 0.01	0.80	1.218
50.39	31.453 ± 4.191	0.005	3.25 ± 0.01	0.80	1.522
55.77	23.075 ± 3.968	0.005	3.22 ± 0.02	0.80	0.634

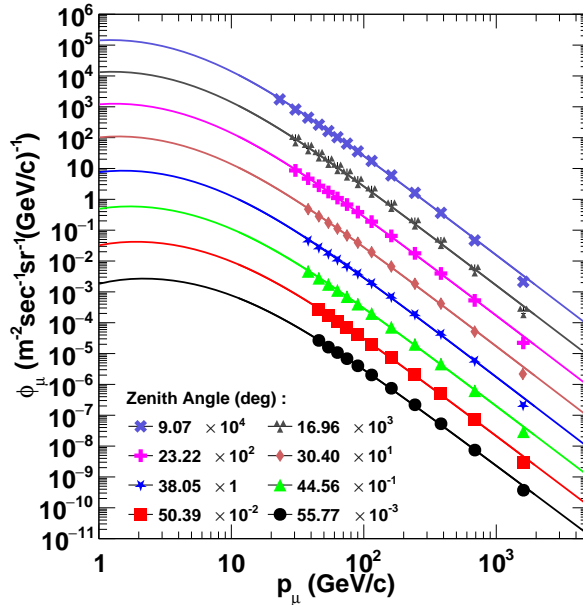


FIGURE 5 The total muon flux at different zenith angles⁵⁴ at an altitude of 450 m is given in right figure. The solid lines are obtained by fitting the data with Eq. 4 keeping $E_0 = 0.005 \text{ GeV/g-cm}^{-2}$ and $k = 0.80 \text{ GeV}$.

be 0.80 GeV and look for the variation in variable E_0 . A higher value of E_0 at 0.005 GeV/g-cm⁻² is required for zenith angle variation.

Figure 5 shows the total muon flux at different zenith angles⁵⁴ at an altitude of 450 m. The solid lines are obtained by fitting the data with Eq. 4 keeping $E_0 = 0.005 \text{ GeV/g-cm}^{-2}$ and $k = 0.80 \text{ GeV}$. The values of parameters of Eq. 4 for different zenith angles are given in Table 5. At zenith angle 9.07° , the integrated flux is $69.77 \text{ m}^{-2} \text{ s}^{-1} \text{ sr}^{-1}$. The integrated flux decreases with increasing zenith angle which is expected as the path length increases with zenith angle. The value of n is almost constant with variation in zenith angle. The parametrization provides a reasonable extrapolation in the 1–30 GeV/c range. Additional low-energy data would improve the description.

4.3 | Variation of Integrated flux with respect to atmospheric depth and zenith angle

As discussed in the previous section, the parametrization of the data helps to get the integrated flux as function of atmospheric depth and zenith angle. Figure 6 (left) shows the variation in integrated negative muon flux with respect to the atmospheric depth. The shape of the curve can be understood as follows. As the primary particles enter the atmosphere they interact with the air molecules and this results in the production of hadrons finally decaying to muons. As the particles travel downwards they encounter more target nuclei and hence the production increases very fast. At a certain depth, the muon flux reaches a maximum, beyond which it begins to decrease. This happens since the produced muons also interact with the atmosphere and decay. Thus the maximum number of muons are found at an atmospheric depth of about 200 gm/cm².

Figure 6 (right) shows the variation in integrated total muon flux with respect to the zenith angle. The integrated muon flux decreases as the zenith angle increases because muons arriving at larger zenith angles travel longer distances through the atmosphere, which increases their probability of interacting and decaying, leading to a lower observed flux.

5 | THE DISTRIBUTION OF ATMOSPHERIC NEUTRINOS

Along with muons and other secondary particles, neutrinos are also produced in the atmosphere during extensive air showers created by primary particles. However, their interaction cross-section is extremely low, allowing them to pass through the

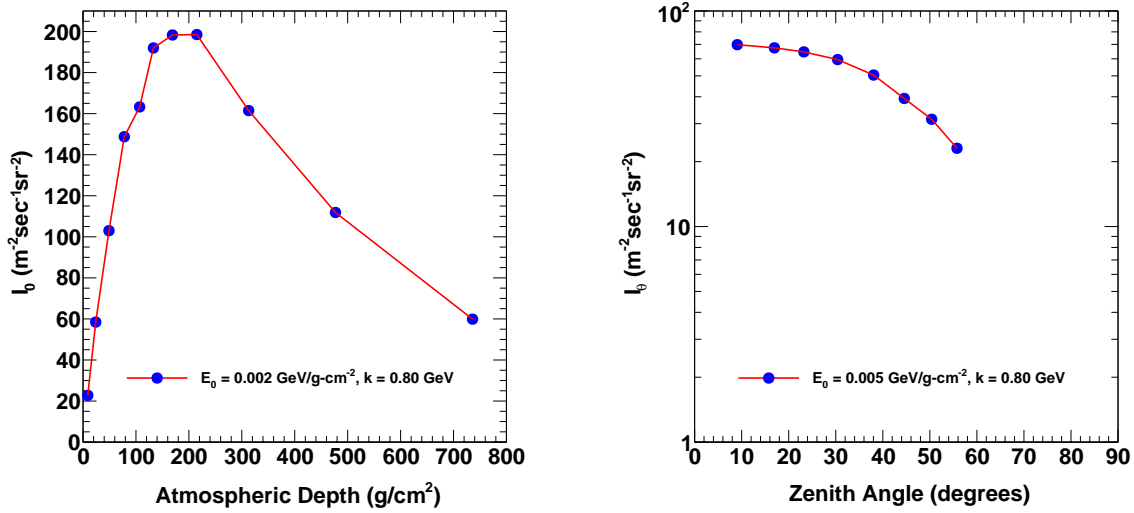


FIGURE 6 Variation in Integrated muon flux with respect to atmospheric depth (left) and zenith angle (right).

atmosphere and Earth with very few interactions. Several big experimental detectors have been developed to measure their properties in various laboratories, such as KamLAND, Gran Sasso, IceCube etc.^{55,56,57,58,59,60,61,62,63} Since the measured energy distributions of neutrinos are scarce, the present analysis employs neutrino flux data generated using the JAM (Jet AA Microscopic) nuclear interaction model, a widely used hadronic interaction framework that reproduces particle yields in cosmic-ray-induced air showers. This simulation takes measured data on primary particle distribution as input and uses known Physics processes. We specifically use the flux datasets provided by Honda et al.⁶⁴, who applied the JAM model to compute the atmospheric neutrino flux at several experimental locations worldwide.

The neutrino flux is parametrized using the following modified energy distribution function:

$$I(E) = I_0 N \left[\frac{E_0 d}{\cos \theta} + E \right]^{-n} \left(1 + \frac{E}{\epsilon} \right)^{-1}. \quad (11)$$

Unlike other secondary particles discussed in the previous sections, such as muons, neutrinos do not decay in the atmosphere. As a result, the decay term has been excluded from the distribution. Instead, we introduce a source term, which accounts for an additional inverse dependence of the neutrino flux on energy, beyond the standard power-law behavior. This term becomes significant for neutrinos with energies exceeding a certain threshold, governed by the parameter ϵ , which effectively encodes the influence of the finite lifetimes of the parent particles that produce the neutrinos.

Figure 7 shows the energy distribution of muon type atmospheric neutrinos (left) and anti-neutrinos (right), simulated for various sites⁶⁴ for $\cos \theta = 0.90 - 1.00$, the solid lines are fits using Eq. 11. Figure 8 shows the same for electron-type neutrinos (and anti-neutrinos). The corresponding fit parameters are listed in Tables 6 and 7. The function in Eq. 11 gives excellent description of all types of neutrinos.

Muon-type neutrinos are mainly produced in the atmosphere through the decay of charged pions and kaons, which generate muons and their associated neutrinos. At higher energies, these mesons have longer lifetimes due to relativistic time dilation and are more likely to interact before decaying, reducing the number of neutrinos produced. Thus the large value of parameter ϵ gives the energy above which the spectrum starts becoming steeper as effectively it makes the spectral index to increase. In contrast, electron-type neutrinos originate primarily from muon decay. Since muons live much longer than their parent mesons, this transition starts at much lower energy giving small ϵ . The parameter I_0 for neutrinos is slightly higher than that for anti-neutrinos at all sites. I_0 for muon-type neutrinos is more than twice of that for electron-type neutrinos. $E_0 d$ is very low for all types of neutrinos. The index n is around 3.00 for muon-type neutrinos, which closely matches the n value for muons and 2.50 for electron-type neutrinos. An analytic function with parameters at different sites can be very useful for detector simulation, saving computational time. The function given by Eq. 11 works well for the energy distribution of neutrinos in all energy range. The data was taken from the simulation at various sites as the actual experimental data for neutrino energy distribution are

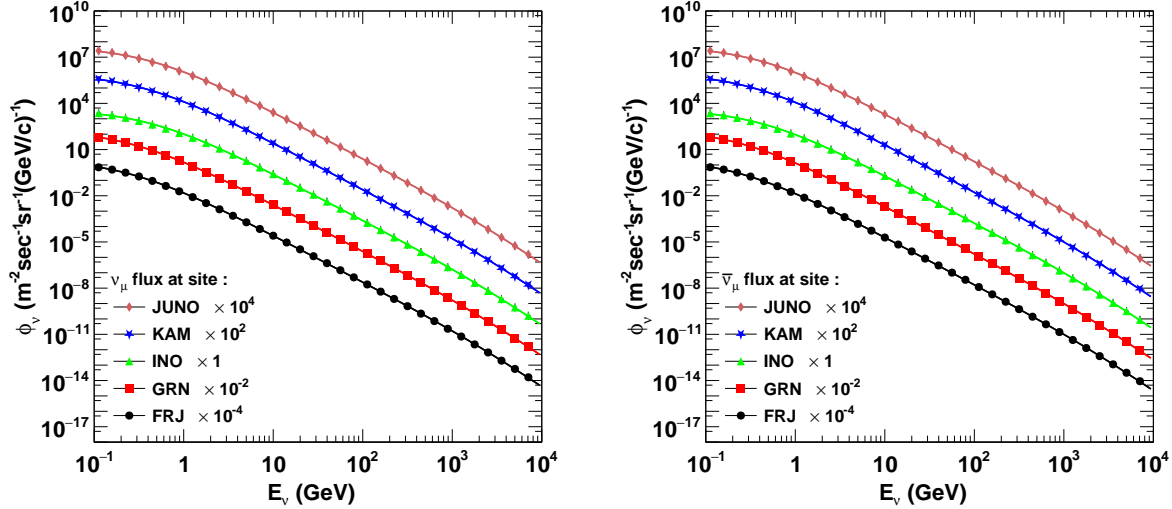


FIGURE 7 The energy distribution of muon type atmospheric neutrinos (left) and anti-neutrinos (right), simulated for various sites⁶⁴ for $\cos \theta = 0.90 - 1.00$, the solid lines are fits using Eq. 11.

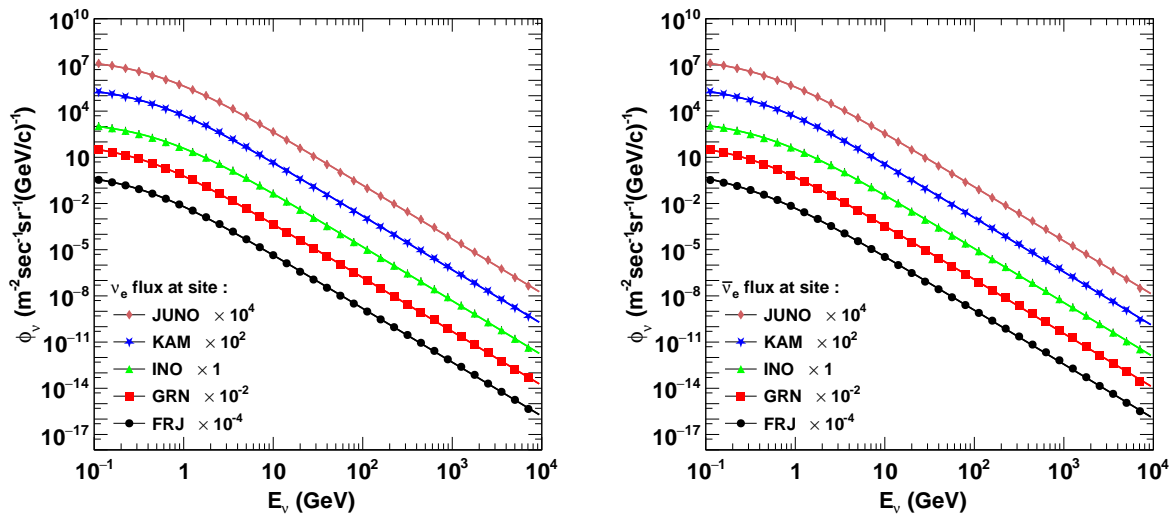


FIGURE 8 The energy distribution of electron type atmospheric neutrinos (left) and anti-neutrinos (right), simulated for various sites⁶⁴ for $\cos \theta = 0.90 - 1.00$, the solid lines are fits using Eq. 11.

scarce. The simulated data sets of neutrinos are obtained using measured primary particle distributions as inputs and detailed simulation including known processes in the atmosphere. These simulated data sets are very well represented by our analytic function which can be useful for detector simulation. In future, measured energy distributions of atmospheric neutrinos (e.g., from Super-Kamiokande) may become available which will be useful to validate the simulation/parametrizations.

TABLE 6 Values of parameters obtained by fitting the simulated data for the muon type atmospheric neutrinos and anti-neutrinos at various sites for $\cos \theta = 0.90 - 1.00$ with Eq. 11.

Site	Particle Type	I_0 (m $^{-2}$ s $^{-1}$ sr $^{-1}$)	$E_{0,d}$ (GeV)	n	ϵ (GeV)	χ^2/NDF
Frejus (45.18°N, 6.69°E)	ν_μ	1312.47 ± 39.57	0.22 ± 0.01	3.02 ± 0.01	2123.34 ± 195.28	0.46
	$\bar{\nu}_\mu$	1291.69 ± 37.95	0.21 ± 0.01	3.09 ± 0.01	2351.15 ± 217.68	0.39
Gran Sasso (42.42°N, 13.51°E)	ν_μ	1209.35 ± 37.18	0.24 ± 0.01	3.03 ± 0.01	2183.32 ± 203.32	0.45
	$\bar{\nu}_\mu$	1188.68 ± 35.57	0.23 ± 0.01	3.09 ± 0.01	2403.84 ± 226.01	0.42
Kamioka (36.42°N, 137.31°E)	ν_μ	829.43 ± 27.76	0.31 ± 0.01	3.04 ± 0.01	2276.77 ± 217.44	0.46
	$\bar{\nu}_\mu$	811.19 ± 26.43	0.30 ± 0.01	3.10 ± 0.01	2453.71 ± 237.91	0.41
JUNO (22.11°N, 112.52°E)	ν_μ	617.34 ± 22.41	0.37 ± 0.01	3.03 ± 0.01	2069.50 ± 200.97	0.95
	$\bar{\nu}_\mu$	600.24 ± 20.98	0.36 ± 0.01	3.09 ± 0.01	2370.01 ± 229.01	0.58
INO (9.96°N, 77.28°E)	ν_μ	550.46 ± 20.68	0.40 ± 0.01	3.03 ± 0.01	2083.80 ± 260.79	1.36
	$\bar{\nu}_\mu$	532.91 ± 19.24	0.38 ± 0.01	3.09 ± 0.01	2339.75 ± 232.85	0.88

TABLE 7 Values of parameters obtained by fitting the simulated data for the electron type atmospheric neutrinos and anti-neutrinos at various sites for $\cos \theta = 0.90 - 1.00$ with Eq. 11.

Site	Particle Type	I_0 (m $^{-2}$ s $^{-1}$ sr $^{-1}$)	$E_{0,d}$ (GeV)	n	ϵ (GeV)	χ^2/NDF
Frejus (45.18°N, 6.69°E)	ν_e	625.73 ± 17.73	0.28 ± 0.02	2.50 ± 0.00	0.29 ± 0.06	2.20
	$\bar{\nu}_e$	561.53 ± 13.39	0.43 ± 0.01	2.52 ± 0.00	0.03 ± 0.00	3.38
Gran Sasso (42.42°N, 13.51°E)	ν_e	570.84 ± 17.55	0.30 ± 0.04	2.50 ± 0.00	0.31 ± 0.09	2.40
	$\bar{\nu}_e$	516.68 ± 26.19	0.33 ± 0.01	2.51 ± 0.00	0.19 ± 0.13	2.83
Kamioka (36.42°N, 137.31°E)	ν_e	378.94 ± 8.85	0.37 ± 0.06	2.50 ± 0.00	0.39 ± 0.16	2.22
	$\bar{\nu}_e$	355.30 ± 8.30	0.47 ± 0.00	2.52 ± 0.00	0.16 ± 0.01	2.92
JUNO (22.11°N, 112.52°E)	ν_e	273.90 ± 6.53	0.35 ± 0.04	2.51 ± 0.01	0.80 ± 0.20	2.90
	$\bar{\nu}_e$	265.90 ± 3.98	0.29 ± 0.02	2.52 ± 0.01	0.87 ± 0.17	2.58
INO (9.96°N, 77.28°E)	ν_e	239.50 ± 3.84	0.34 ± 0.03	2.51 ± 0.01	1.01 ± 0.18	3.13
	$\bar{\nu}_e$	238.22 ± 3.44	0.29 ± 0.02	2.52 ± 0.01	1.02 ± 0.17	2.44

6 | SUMMARY AND PROSPECTS

In this work, we presented analytical formulations to describe the momentum distribution of primary and secondary cosmogenic particles. Although distributions of different particles are described by power law, their modification terms are different depending on their interaction. We begin by modifying the power-law distribution and incorporating terms that account for energy loss at lower energies for both primary and secondary particles. For primary particles such as protons and helium, a $1/E$ term is introduced to account for flux loss. For secondary particles such as muons, an exponentially decaying factor is included to reflect their finite lifetime. Additionally, these modified formulations incorporate parameters such as d (atmospheric depth) and θ (zenith angle) to account for variations in flux with altitude and zenith angle. It is shown that the presence of decay term does not affect the zenith angle distribution of muons. We fit various experimental data at sea level as well as at different altitudes and zenith angles in terms of parameters of the proposed analytical functions. Furthermore, we extend our parametrization to atmospheric muon and electron-type neutrinos by introducing a source term instead of a decay function which are applied on simulated data. The proposed functions successfully describe the momentum distributions of primary cosmic particles as well as secondary particles such as muons and neutrinos. The functions are useful for obtaining integrated flux for different cases and as inputs for detector simulations. These formulations can be extended to other cosmogenic particles, such as charm-induced leptons (prompt muons and neutrinos) from decays of D -mesons and Λ_c -baryons, and to high-energy photons from neutral pion decay. Similar analytical treatments may also apply to heavier primary nuclei beyond helium. The present parametrizations are valid within the measured energy range and effects like geomagnetic cutoffs etc. are absorbed in the fitted parameters.

FINANCIAL DISCLOSURE

No financial support has been used for this work

CONFLICT OF INTEREST

The authors declare no potential conflict of interests.

References

1. Hess VF. Über Beobachtungen der durchdringenden Strahlung bei sieben Freiballonfahrten. *Phys. Z.* 1912;13:1084–1091.
2. Pacini D. La radiazione penetrante alla superficie ed in seno alle acque. *Il Nuovo Cimento.* 1912;3(1):93-100. doi: 10.1007/BF02957440
3. KOLHORSTER W. Messungen der durchdringenden Strahlung im Freiballon in grosseren Hohen. *Phys. Zeits.* 1913;14:1153-1156.
4. Millikan RA, Bowen IS. High Frequency Rays of Cosmic Origin I. Sounding Balloon Observations at Extreme Altitudes. *Phys. Rev.* 1926;27:353–361. doi: 10.1103/PhysRev.27.353
5. Millikan RA, Otis RM. High Frequency Rays of Cosmic Origin II. Mountain Peak and Airplane Observations. *Phys. Rev.* 1926;27:645–658. doi: 10.1103/PhysRev.27.645
6. Millikan RA, Cameron GH. The Origin of the Cosmic Rays. *Phys. Rev.* 1928;32:533–557. doi: 10.1103/PhysRev.32.533
7. Rossi B. *Cosmic Rays*. McGraw-Hill paperbacks in physicsMcGraw-Hill, 1964.
8. Group PD, Workman RL, Burkert VD, et al. Review of Particle Physics. *Progress of Theoretical and Experimental Physics.* 2022;2022(8):083C01. doi: 10.1093/ptep/ptac097
9. Maeno T, Orito S, Matsunaga H, et al. Successive measurements of cosmic-ray antiproton spectrum in a positive phase of the solar cycle. *Astroparticle Physics.* 2001;16(2):121-128. doi: [https://doi.org/10.1016/S0927-6505\(01\)00107-4](https://doi.org/10.1016/S0927-6505(01)00107-4)
10. Shikaze Y, Haino S, Abe K, et al. Measurements of 0.2–20GeV/n cosmic-ray proton and helium spectra from 1997 through 2002 with the BESS spectrometer. *Astroparticle Physics.* 2007;28(1):154–167. doi: <https://doi.org/10.1016/j.astropartphys.2007.05.001>
11. Panov AD, Adams JH, Ahn HS, et al. Energy spectra of abundant nuclei of primary cosmic rays from the data of ATIC-2 experiment: Final results. *Bulletin of the Russian Academy of Sciences, Physics.* 2009;73(5):564–567. doi: 10.3103/S1062873809050098
12. Panov AD, Adams JH, Ahn HS, et al. The results of ATIC-2 experiment for elemental spectra of cosmic rays. *arXiv e-prints.* 2006:astro-ph/0612377. doi: 10.48550/arXiv.astro-ph/0612377
13. Adriani O, Barbarino GC, Bazilevskaya GA, et al. PAMELA Measurements of Cosmic-Ray Proton and Helium Spectra. *Science.* 2011;332(6025):69. doi: 10.1126/science.1199172
14. Aguilar M, Alcaraz J, Allaby J, et al. The Alpha Magnetic Spectrometer (AMS) on the International Space Station: Part I – results from the test flight on the space shuttle. *Physics Reports.* 2002;366(6):331–405. doi: [https://doi.org/10.1016/S0370-1573\(02\)00013-3](https://doi.org/10.1016/S0370-1573(02)00013-3)
15. Aguilar M, Aisa D, Alpat B, et al. Precision Measurement of the Proton Flux in Primary Cosmic Rays from Rigidity 1 GV to 1.8 TV with the Alpha Magnetic Spectrometer on the International Space Station. *Phys. Rev. Lett.* 2015;114:171103. doi: 10.1103/PhysRevLett.114.171103
16. Aguilar M, Aisa D, Alpat B, et al. Precision Measurement of the Helium Flux in Primary Cosmic Rays of Rigidities 1.9 GV to 3 TV with the Alpha Magnetic Spectrometer on the International Space Station. *Phys. Rev. Lett.* 2015;115:211101. doi: 10.1103/PhysRevLett.115.211101
17. Ahn HS, Allison P, Bagliesi MG, et al. Energy Spectra of Cosmic-ray Nuclei at High Energies. *apj.* 2009;707(1):593-603. doi: 10.1088/0004-637X/707/1/593
18. Ahn HS, Allison P, Bagliesi MG, et al. Discrepant Hardening Observed in Cosmic-ray Elemental Spectra. *apjl.* 2010;714(1):L89-L93. doi: 10.1088/2041-8205/714/1/L89
19. Ryan MJ, Ormes JF, Balasubrahmanyam VK. Cosmic ray proton and helium spectra above 50 gev. *Phys. Rev. Lett.* 1972;28:985–988. [Erratum: *Phys. Rev. Lett.* 28, 1497 (1972)]doi: 10.1103/PhysRevLett.28.985
20. Bocciolini M, Celletti F, Finetti N, et al. The WiZard/CAPRICE silicon-tungsten calorimeter. *Nuclear Instruments and Methods in Physics Research Section A: Accelerators, Spectrometers, Detectors and Associated Equipment.* 1996;370(2):403-412. doi: [https://doi.org/10.1016/0168-9002\(95\)00841-1](https://doi.org/10.1016/0168-9002(95)00841-1)
21. Boezio M, Carlson P, Francke T, et al. The Cosmic-Ray Antiproton Flux between 0.62 and 3.19 GeV Measured Near Solar Minimum Activity. *apj.* 1997;487(1):415-423. doi: 10.1086/304593
22. Boezio M, Carlson P, Francke T, et al. The Cosmic-Ray Proton and Helium Spectra between 0.4 and 200 GV. *apj.* 1999;518(1):457-472. doi: 10.1086/307251
23. Asakimori K, Burnett TH, Cherry ML, et al. Cosmic-Ray Proton and Helium Spectra: Results from the JACEE Experiment. *apj.* 1998;502(1):278-283. doi: 10.1086/305882

24. Grieder P. *Cosmic Rays at Earth*. Elsevier Science, 2001.

25. Bethe H, Heitler W. On the Stopping of fast particles and on the creation of positive electrons. *Proc. Roy. Soc. Lond. A.* 1934;146:83–112. doi: 10.1098/rspa.1934.0140

26. Gaisser TK, Engel R, Resconi E. *Cosmic Rays and Particle Physics: 2nd Edition*. Cambridge University Press, 2016.

27. Gaisser TK. Semianalytic approximations for production of atmospheric muons and neutrinos. *Astropart. Phys.* 2002;16:285–294. doi: 10.1016/S0927-6505(01)00143-8

28. Pan X, Yuan Q. Injection spectra of different species of cosmic rays from AMS-02, ACE-CRIS and Voyager-1. *Res. Astron. Astrophys.* 2023;23:115002. doi: 10.1088/1674-4527/acf443

29. Allkofer OC, Carstensen K, Dau DW. The absolute cosmic ray muon spectrum at sea level. *Phys. Lett. B.* 1971;36:425–427. doi: 10.1016/0370-2693(71)90741-6

30. Ayre CA, Baxendale JM, Daniel BJ, et al. THE ABSOLUTE MUON SPECTRUM IN THE RANGE 3.5-GEV/C - 700-GEV/C. (TALK). In: 1973.

31. Lipari P. Lepton spectra in the earth's atmosphere. *Astropart. Phys.* 1993;1:195–227. doi: 10.1016/0927-6505(93)90022-6

32. Maeda K. Energy and zenith angle dependence of atmospheric muons. *Fortsch. Phys.* 1973;21:113–154. doi: 10.1002/prop.19730210302

33. Stephens SA. CHARGE RATIO OF MUONS AT SEA LEVEL AND ITS DEPENDENCE ON ZENITH ANGLES.. In: 1979:96–101.

34. Heck D, Knapp J, Capdevielle JN, Schatz G, Thouw T. CORSIKA: A Monte Carlo code to simulate extensive air showers. 1998.

35. Sogarwal H, Shukla P. Inclusive fluxes of secondary air-shower particles. *JCAP*. 2024;08:013. doi: 10.1088/1475-7516/2024/08/013

36. Fedynitch A, Woodley W, Piro MC. On the Accuracy of Underground Muon Intensity Calculations. *Astrophys. J.* 2022;928(1):27. doi: 10.3847/1538-4357/ac5027

37. Azarkin MY, Kirakosyan MR, Meshkov OV, Ryabov VA, Shepetov AL. Reconstructing the Energy Spectrum of Cosmic Muons Measured with the Underground Detector of the Tien Shan High-Altitude Station. *Bull. Lebedev Phys. Inst.* 2024;51(5):166–173. doi: 10.3103/S1068335624600281

38. Woodley W, Fedynitch A, Piro MC. Cosmic ray muons in laboratories deep underground. *Phys. Rev. D.* 2024;110(6):063006. doi: 10.1103/PhysRevD.110.063006

39. Sato H, Kin T, Giammanco A. Measurement of energy differential spectrum of cosmic-ray muons below 400 MeV. *Journal of Instrumentation*. 2022;17(08):P08009.

40. Adamson P, Andreopoulos C, Arms KE, et al. Observation of muon intensity variations by season with the MINOS far detector. *Phys. Rev. D.* 2010;81:012001. doi: 10.1103/PhysRevD.81.012001

41. Adamson P, Mualem L, Newman HB, Orchanian M, Patterson RB, Collaboration M. Observation of seasonal variation of atmospheric multiple-muon events in the MINOS Near and Far Detectors. *Physical Review D.* 2015;91(11). doi: 10.1103/PhysRevD.91.112006

42. Abbasi R, Ackermann M, Adams J, et al. Observation of seasonal variations of the flux of high-energy atmospheric neutrinos with IceCube. *European Physical Journal C.* 2023;83(9):777. doi: 10.1140/epjc/s10052-023-11679-5

43. IceCube Collaboration , Abbasi R, Ackermann M, et al. Seasonal variations of the atmospheric muon neutrino spectrum measured with IceCube. *European Physical Journal C.* 2025;85(12):1368. doi: 10.1140/epjc/s10052-025-14844-0

44. Shukla P, Sankrith S. Energy and angular distributions of atmospheric muons at the Earth. *Int. J. Mod. Phys. A.* 2018;33(30):1850175. doi: 10.1142/S0217751X18501750

45. Haino S, Sanuki T, Abe K, et al. Measurements of primary and atmospheric cosmic-ray spectra with the BESS-TeV spectrometer. *Physics Letters B.* 2004;594(1):35–46. doi: <https://doi.org/10.1016/j.physletb.2004.05.019>

46. Rastin BC. AN ACCURATE MEASUREMENT OF THE SEA LEVEL MUON SPECTRUM WITHIN THE RANGE 4-GEV/C TO 3000-GEV/C. *J. Phys. G.* 1984;10:1609–1628. doi: 10.1088/0305-4616/10/11/017

47. Gardener M, Jones DG, Taylor FE, Wolfendale AW. The Momentum Spectrum of Cosmic Ray Muons near Sea Level in the Momentum Range 0.4-10 GeV/c. *Proceedings of the Physical Society*. 1962;80(3):697. doi: 10.1088/0370-1328/80/3/314

48. Hayman PJ, Wolfendale AW. The Momentum Spectrum of Cosmic Ray Muons near Sea Level in the Momentum Range 5-1000 GeV/c. *Proceedings of the Physical Society*. 1962;80(3):710. doi: 10.1088/0370-1328/80/3/315

49. De Pascale MP, Morselli A, Picozza P, et al. Absolute spectrum and charge ratio of cosmic ray muons in the energy region from 0.2 GeV to 100 GeV at 600 m above sea level. *Journal of Geophysical Research: Space Physics*. 1993;98(A3):3501–3507. doi: <https://doi.org/10.1029/92JA02672>

50. Jokisch H, Carstensen K, Dau WD, Meyer HJ, Allkofer OC. Cosmic-ray muon spectrum up to 1 TeV at 75° zenith angle. *Phys. Rev. D.* 1979;19:1368–1372. doi: 10.1103/PhysRevD.19.1368

51. Kremer J, Boezio M, Ambriola ML, et al. Measurements of Ground-Level Muons at Two Geomagnetic Locations. *Phys. Rev. Lett.*. 1999;83:4241–4244. doi: 10.1103/PhysRevLett.83.4241
52. Sogarwal, Hariom and Shukla, Prashant . Measurement of atmospheric muon angular distribution using a portable setup of liquid scintillator bars. *JCAP*. 2022;07(07):011. doi: 10.1088/1475-7516/2022/07/011
53. Bellotti R, Cafagna F, Circella M, et al. Measurement of the negative muon spectrum between 0.3 and 40 GeV/c in the atmosphere. *Phys. Rev. D*. 1996;53:35–43. doi: 10.1103/PhysRevD.53.35
54. Achard P, Adriani O, Aguilar-Benitez M, et al. Measurement of the atmospheric muon spectrum from 20 to 3000 GeV. *Physics Letters B*. 2004;598(1):15–32. doi: <https://doi.org/10.1016/j.physletb.2004.08.003>
55. Hirata K, Kajita T, Koshiba M, et al. Experimental study of the atmospheric neutrino flux. *Physics Letters B*. 1988;205(2):416–420. doi: [https://doi.org/10.1016/0370-2693\(88\)91690-5](https://doi.org/10.1016/0370-2693(88)91690-5)
56. Barr G, Gaisser TK, Stanev T. Flux of Atmospheric Neutrinos. *Phys. Rev. D*. 1989;39:3532–3534. doi: 10.1103/PhysRevD.39.3532
57. Becker-Szendy R, Bratton CB, Casper D, et al. Search for muon neutrino oscillations with the Irvine-Michigan-Brookhaven detector. *Phys. Rev. Lett.*. 1992;69:1010–1013. doi: 10.1103/PhysRevLett.69.1010
58. Becker-Szendy R, Bratton C, Casper D, et al. Neutrino measurements with the IMB director. *Nuclear Physics B - Proceedings Supplements*. 1995;38(1):331–336. Neutrino 94doi: [https://doi.org/10.1016/0920-5632\(94\)00765-N](https://doi.org/10.1016/0920-5632(94)00765-N)
59. Agrawal V, Gaisser TK, Lipari P, Stanev T. Atmospheric neutrino flux above 1-GeV. *Phys. Rev. D*. 1996;53:1314–1323. doi: 10.1103/PhysRevD.53.1314
60. Fukuda Y, Hayakawa T, Ichihara E, et al. Study of the atmospheric neutrino flux in the multi-GeV energy range. *Physics Letters B*. 1998;436(1):33–41. doi: [https://doi.org/10.1016/S0370-2693\(98\)00876-4](https://doi.org/10.1016/S0370-2693(98)00876-4)
61. Aartsen MG, Ackermann M, Adams J, et al. Observation of High-Energy Astrophysical Neutrinos in Three Years of IceCube Data. *Phys. Rev. Lett.*. 2014;113:101101. doi: 10.1103/PhysRevLett.113.101101
62. Aartsen MG, Ackermann M, Adams J, et al. The IceCube Neutrino Observatory: instrumentation and online systems. *Journal of Instrumentation*. 2017;12(3):P03012. doi: 10.1088/1748-0221/12/03/P03012
63. Yu S. Measurement of Atmospheric Muon Neutrino Disappearance Using CNN Reconstructions with IceCube. *Physical Sciences Forum*. 2023;8(1). doi: 10.3390/psf2023008062
64. Honda M, Kajita T, Kasahara K, Midorikawa S. Improvement of low energy atmospheric neutrino flux calculation using the JAM nuclear interaction model. *Phys. Rev. D*. 2011;83:123001. doi: 10.1103/PhysRevD.83.123001